Surface & Coatings Technology 492 (2024) 131204

Contents lists available at ScienceDirect

Surface & Coatings Technology

journal homepage: www.elsevier.com/locate/surfcoat

The effects of laser peening on the oxidation behavior of pure titanium at 750 °C

Zachary Brown [a], Nicholas Brooks [a], Roxana Family [b], Mark Weaver [c], Keivan Davami [a,*]

[a] University of Alabama, Department of Mechanical Engineering, Tuscaloosa, AL, USA
[b] University of Pennsylvania, Department of Materials Engineering, Philadelphia, PA, USA
[c] University of Alabama, Department of Metallurgical and Materials Engineering, Tuscaloosa, AL, USA

ARTICLE INFO

Keywords:
Laser peening
High temperature oxidation
Titanium
Thermogravimetric analysis

ABSTRACT

Pure titanium and titanium alloys are essential materials for structural applications due to their high specific strength and corrosion resistance. However, at temperatures above 550–600 °C, an unprotective oxide layer forms, promoting oxygen diffusion and degradation of material properties. Enhancement of titanium's oxidation resistance lies in creating a stable and protective oxide layer on its surface which can be achieved through controlled manufacturing, microalloying, or post processing via surface engineering treatments. In this study, laser peening has been employed to improve the high-temperature oxidation resistance of pure titanium. Two laser-peened and two un-peened titanium specimens were subjected to oxidation in an environment consisting of 21 % oxygen and 79 % argon at 750 °C for 100 h using thermogravimetric analysis. Characterization techniques such as optical and electron microscopy, micro- and nano-indentation, and Raman spectroscopy were employed to analyze the α-case and oxide scale formed during exposure to oxygen at high temperature. The results reveal that laser peening modified the surface characteristics of pure titanium and improved its oxidation resistance. On average, laser peened specimens experienced a 22.3 % reduction in mass gain following oxidation. The study sheds light on mechanisms responsible for this phenomenon, providing valuable insights into the development of novel surface engineering techniques for titanium and its alloys.

1. Introduction

Titanium is a lightweight metal that is well known for its unique characteristics and wide applicability. At room temperature, titanium forms a passive and thin oxide layer which provides exceptional resistance to corrosion and promotes biocompatibility with the human body [1]. Additionally, the metal and its alloys provide remarkable strength to weight ratios, high fracture toughness, and favorable thermal characteristics making it a choice material for many applications where other materials are not practical [1–4]. As such, titanium and its alloys have a significant presence in the aerospace, automotive, and biomedical industries [1–3]. Thermal attributes also make titanium suitable for various high temperature applications, including airframe and aircraft engine parts, heat exchangers, and high-temperature equipment [5–8]. However, at temperatures above 550 °C, titanium will react with oxygen, nitrogen, and other environmental elements, leading to surface oxidation and embrittlement [9,10].

Titanium has been shown to react with oxygen at 1200 °C in air and 610 °C in pure oxygen to form titanium dioxide (TiO_2) [11]. The formation of this TiO_2 oxide layer on the surface of titanium is accompanied by the inward diffusion of oxygen into the substrate itself, which leads to the formation and growth of an oxygen-enriched metal layer known as the "α-case" layer [12–14]. This brittle layer, which forms beneath the TiO_2 oxide scale, can be detrimental to mechanical properties of the material, such as ductility, fracture toughness, and fatigue life [15–17]. Additionally, the growth of an imperfect oxide layer promotes inconsistent oxygen diffusion and the formation of a non-uniform α-case layer. This can result in poor mechanical properties, impaired weldability, non-uniform surface hardness, and susceptibility to corrosion [15,18,19]. The layer also compromises the metal's structural integrity, making it more prone to cracking. In welding applications, this results in the embrittlement of welds, reducing the overall weld quality and joint strength. Non-uniformity in the thickness of the α-case layer can lead to poor corrosion resistance in regions where the α-case layer is thinner. This limits applications of the metal within specific industries where corrosion resistance is of importance, making it challenging to

* Corresponding author.
E-mail address: kdavami@eng.ua.edu (K. Davami).

https://doi.org/10.1016/j.surfcoat.2024.131204
Received 8 June 2024; Received in revised form 2 August 2024; Accepted 4 August 2024
Available online 9 August 2024

predict the metal's mechanical properties accurately and increasing the risk of unexpected failures [18,19]. Titanium alloys that have developed an α-case have also been shown to exhibit less elastic deformation in their crack initiation areas [15].

Improving the high-temperature oxidation resistance of titanium and titanium alloys can be achieved through a variety of techniques including: chemical treatments, such as ion implantation [20–24], physical vapor deposition of ceramic coatings [24], pack cementation [25], pre-oxidation [14], and mechanical surface engineering treatments such as laser peening (LP) [12,26,27] and shot peening (SP) [12,27,28]. However, many coatings are not stable enough for long-term high-temperature applications, and adding alloying elements can change the mechanical behavior and degrade the toughness and ductility of alloy systems [9,10]. Additionally, it is sometimes more practical to treat specimens after they have been manufactured rather than during. That is when post processing surface engineering treatments like LP and SP, which do not alter the bulk material properties of metals and alloys, are typically utilized. These surface engineering techniques are typically used to enhance the mechanical and electrochemical properties of materials through the introduction of high magnitude compressive residual stresses (CRSs) and subsequently a high density of dislocations which can result in grain refinement, twinning, and the formation of sub-grains amongst other things [29]. LP is an alternate peening method and is used as a substitute for traditional SP in certain applications [30,31]. The advantages of LP over conventional SP include the generation of CRSs up to greater depths [26,29,31] and increased flexibility over processing conditions [29].

In recent years, LP and SP have also been shown to influence the high-temperature oxidation of titanium and titanium alloys [12,26–28]. In one study by Kanjer et al. [28] the impact of SP on the high-temperature oxidation behavior of pure titanium was investigated. The impact of SP treatment duration (ranging from 10 to 30 min) has been investigated, revealing that longer treatment durations yield notable effects. Compared to un-treated specimens, the oxidation resistance of SPed specimens demonstrated a significant improvement, with a reduction in mass gain ranging from approximately 30 % to 45 %. Their findings indicated that SP effectively enhanced the oxidation resistance of pure titanium at 700 °C. This improvement was attributed to two main factors: (1) the rapid formation of a nitride layer between the α-case area and the oxide layer, and (2) microstructural modifications, including grain refinement and twinning resulting from the severe plastic deformation imparted by SP. In a more recent study by Kanjer et al. [26], the influence of LP on the high-temperature oxidation behavior of the same metal (99.8 % pure titanium) at the same temperature (700 °C) was also investigated. Their results indicated a reduction in mass gain for LPed specimens and the formation of an adhesive and dense oxide layer without spallation. They also found a decrease in the thickness of the α-case following LP, which promoted the growth of a stoichiometric and dense rutile layer of TiO_2 that increased nitrogen diffusion through oxidation. In a similar study by Lavisse et al. [12], the role of nitrogen was explored following LP and SP and long-term (3000 h) high-temperature oxidation of commercially-pure titanium plates at 700 °C in an air environment. The results from this study revealed that both surface treatments resulted in alterations to the microstructure of titanium. Their main observation was a significant increase in the density of twins in the SPed specimens, whereas the LPed specimens exhibited a relatively lower density of twins. At 700 °C in air, both un-treated and SPed specimens experienced spallation of the oxide layer after approximately 1700 h of exposure. However, in the case of LPed specimens, this phenomenon was not observed even after 3000 h of exposure. This was attributed to the development of a denser, more compact, and more adherent oxide scale, which reduced the extent of α-case formation following LP as compared to SP. This outcome is highly advantageous as it helps prevent undesirable oxygen diffusion into the titanium, which is crucial for preserving the metal's ductility. A similar study conducted by Optasanu et al. [27] was performed to compare the high-temperature oxidation of Ti-Beta-21S following both LP and SP. During oxidation in a pure oxygen environment, the mass gain initially follows a purely parabolic trend for approximately 10 h, with no notable distinction between un-treated and treated specimens. However, in both treated and un-treated specimens, the oxide scale develops distinct layers for longer durations, resulting in an almost linear increase in mass gain. Notably, the SPed specimens exhibit a higher oxidation rate than un-treated and LPed specimens. However, in air, defects and the higher density of grain boundaries introduced through mechanical surface treatments facilitated the diffusion of larger quantities of nitrogen, which reduced the mobility of oxygen. This contributed to the improved oxidation resistance of Ti-Beta-21S subjected to SP and LP treatments. This observation highlights the significant influence of atmospheric nitrogen in the high-temperature oxidation process of Ti-Beta-21S in an air environment [27].

While previous studies have shown that LP can be effective in improving the oxidation resistance of titanium and titanium alloys in dry air [12,21,26,27,32,33], the impact of LP on the oxidation behavior in atmospheres devoid of nitrogen has not been investigated thoroughly. While the work by Kanjer et al. [21] showed the viability of LP to reduce oxidation of pure titanium at 700 °C in a pure oxygen atmosphere through thermogravimetric analysis (TGA), the focus of their work was on investigating the results from dry air experiments, and no further experimentation was conducted involving specimens oxidized in pure oxygen. Moreover, no studies that have investigated the high-temperature oxidation behavior of titanium in nitrogen-free atmospheres have explored the impact of LP on non-sheet materials, nor has any research examined the repeatability and consistency of the oxidation kinetics – factors that could be crucial in applications pertaining to this research. Additionally, the oxidation behavior of LPed titanium has only been studied for LP treatments that were performed using aluminum tape as ablative layers. This research examines how the high-temperature oxidation behavior of pure (Grade 1) titanium specimens was affected by LP using vinyl tape as the ablative layer.

In this study, two un-peened (UPed) and two LPed specimens were examined before and after high-temperature oxidation. The specimens were subjected to a temperature of 750 °C for oxidation periods lasting 100 h. Various characterization techniques such as scanning electron microscopy (SEM), optical microscopy (OM), and microindentation were employed to evaluate the microstructure and mechanical properties following surface treatment. Then, the oxidation kinetics were analyzed using TGA. After high-temperature oxidation, further analysis was conducted using OM, SEM, microindentation, nanoindentation, and Raman spectroscopy to investigate differences in the oxidation mechanics between the un-treated and LPed specimens. Furthermore, nanoindentation results were used to draw quantitative conclusions regarding the effects of the LP treatment on oxygen diffusivity at high temperatures and Raman spectroscopy was used to quantify the increase in density of the formed oxide layer – both relationships not utilized in previous work regarding the oxidation of LPed titanium.

2. Methodology

2.1. Materials

The material evaluated in this research was Grade 1 titanium obtained from Goodfellow Corp. Rectangular bars with a 10 × 12 mm^2 cross section with the chemical composition included in Table 1 were used. The equiaxed microstructure of the pure titanium suggests that it was annealed around 700 °C for up to 2 h in air [34,35]. The material was cut using electric discharge machining (EDM) to dimensions of 10 × 5 × 5 mm^3 to create specimens that met the necessary size requirements for TGA. Another set of specimens were cut with EDM to dimensions of 10 × 12 × 15 mm^3 to be used in the investigation of the effects of LP before high-temperature oxidation. Excluding specimens used for profilometry, all specimens were ground to a smooth surface with P1200

Table 1
Chemical composition of the Grade 1 titanium used in this study (wt%).

Elements	Ti	Al	Cr	Mn	Ni	V	Fe	Si	Cu	Sn
wt%	Bal.	0.05	0.05	0.05	0.05	0.05	0.03	0.02	0.02	0.02

grit SiC grinding paper (before LP on LPed specimens). The larger specimens were peened on one face, while the smaller specimens (used for TGA) were peened on all six faces. TGA specimens had their edges slightly chamfered before oxidation to minimize the interaction of perpendicularly growing oxide layers.

Less than 0.01 wt% Mg, Ta, and Co.

2.2. Laser peening treatment

The LP process utilizes a high-energy pulsed laser to impact the surface of the material. Upon impact, a plasma plume is generated at the surface of the material, which is covered with an ablative overlay (vinyl tape in this case) and a thin layer of water. This plasma plume is then confined at the surface of the material by the water overlay which directs the pressure generated by the plasma plume into the material. This pressure pulse causes plastic deformation within the material that is counteracted by an elastic-plastic response, resulting in high-magnitude CRSs. These CRSs imparted by LP have been detected up to depths of ~2–3 mm below metals' peened surface [29,36].

In this research, LP treatment was performed with a Continuum Powerlite DLS pulsed laser operating at a wavelength of 1064 nm and pulse duration (at full-width half maximum) of 8 ns. The treatment was conducted at a laser energy of 2.5 J using a circular spot with a diameter of ~2 mm. As calculated from these parameters, a laser power density of 10 GW/cm^2 is obtained. The shots were placed such that there was a 30 % overlap between successive shots. The path of alternating horizontal rows of shots was created by maneuvering the laser in the transverse and longitudinal directions. Vinyl tape was used as an ablative layer, and flowing water was used as the confining layer. A schematic of the LP process is included in Fig. 1.

2.3. Mass gain measurements

To investigate the effect of the LP treatment on the mass gain and oxidation related kinetics of the pure (Grade 1) Ti, specimens were prepared for TGA in two conditions: UPed (specimens UP-A and UP-B) and LPed (specimens LP-A and LP-B). The LPed specimens had been LPed on all six surfaces. Two specimens of each type were prepared to evaluate the repeatability of the results. TGA of the specimens was performed using a TGA analyzer (TGA, LABSYS evo, Setaram Instruments). Specimens were heated to 750 °C at a heating rate of 30 °C/min and held at that temperature for 100 h. Between 400 °C and 700 °C, titanium experiences cubic and parabolic oxidation rates [16], however, the oxidation of titanium has been reported to obey a parabolic rate equation between 600 °C and 1000 °C [37]. Testing was conducted in this regime to facilitate comparative elucidation of the influence of surface modification on the high temperature oxidation behavior of titanium. By utilizing a temperature of 750 °C, the transition from parabolic to linear mass gain is visible during TGA and creates a clear distinction between protective and non-protective oxidation characteristics. In order to evaluate the individual role of oxygen in the diffusion and oxide formation processes, the analysis was carried out in a controlled atmosphere composed of argon and oxygen flowing at rates of 15.8 mL/min and 4.2 mL/min, respectively, to mimic the oxygen content in atmospheric air.

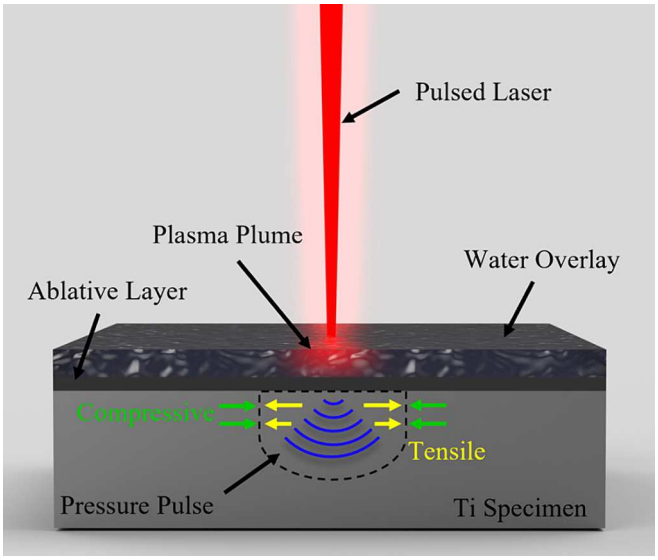

Fig. 1. Illustration of the laser peening process.

2.4. Optical and electron microscopy analysis

To observe the cross-section of specimens following treatment, oxidized specimens were mounted in a conductive resin and cut using a low-speed wafering saw (Isomet High Speed Pro, Buehler). Specimens that had not been oxidized were cut using EDM. All specimen cross-sections were ground using P220–P2400 grit SiC grinding papers, then polished with 3–1 μm diamond suspensions and 0.05 μm colloidal silica for SEM and OM imaging purposes. Cross-sections of un-oxidized and oxidized specimens were etched with Kroll's reagent (95 % H_2O, 3 % HNO_3, 2 % HF) for 2–5 s to reveal grain boundaries and features within the microstructure. Optical microscopy was carried out using a Keyence VHX-7000 digital microscope using full and partial coaxial lighting modes. SEM was performed using a Thermo-Fisher Scientific Apreo 2 scanning electron microscope. All SEM micrographs were obtained using the secondary electron mode with an Everhart-Thornley detector and a beam voltage of 20 keV and a beam current of 3.2 nA.

To observe the LPed surface and resulting microstructure before oxidation, a pre-polished surface (ground with P220–P2400 grit SiC grinding papers, then polished with 3–1 μm diamond suspensions and 0.05 μm colloidal silica) was prepared before LP. After LP, the surface was imaged using the high dynamic range (HDR) mode on the Keyence VHX-7000 digital microscope, without any additional surface preparation following the LP process.

2.5. Microhardness analysis

Microindentation tests were carried out to evaluate the increased microhardness and effective depth of LP in un-oxidized specimens. For oxidized specimens, microhardness was used to characterize the depth of the α-case layer and evaluate the resulting increase in hardness. Measurements were taken at various depths along the cross sections of the specimens. Specimens were evaluated using an automated microhardness tester (MMT-X7B, Clemex) with a diamond pyramid Vickers indenter tip. A force of ~0.25 N (25 gf) and a dwell time of 10 s was used to create an 8 × 15 matrix of indents at varying depths from the surface. The distance between each row and column of indents was 30 μm. To avoid effects from the free surface, indents were started ~40 μm from the surface. These parameters were used for the evaluation of both un-oxidized and oxidized specimens.

2.6. Nanohardness analysis

To better understand the local characteristics of the α-case layer and more accurately calculate diffusion coefficients, oxidized specimens were studied using an Anton Paar NHT^3 nanoindentation tester with a diamond Berkovich indenter. The indents were performed using linear loading with loading and unloading rates of 400 mN/min and a 10 s dwell time at a maximum load of 200 mN. Indents at various depths from the surface were laid out in 3 × 10 matrices with 25 μm between each row and column. Nanoindentation was performed at 3 different locations on the LPed and UPed specimens.

2.7. X-ray diffraction residual stress measurements

To quantify the residual stresses generated on the surface of the material from the LP process, x-ray diffraction (XRD) residual stress analysis has been performed. XRD was performed with Pulstec micro-X360s residual stress analyzer. Stress calculations were made using the cos(α) technique, utilizing the full ring of x-ray back diffraction. For the measurements, a Young's modulus of 116 GPa and a Poisson's ratio of 0.32 were used. A Vanadium X-ray tube was chosen to analyze diffraction from the (103) plane in Titanium and utilized a diffraction angle of 140°. The x-ray spot size was approximately 2 mm in diameter with a penetration depth of a couple micrometers. To minimize measurement errors resulting from large grain size, an oscillation on Ψ angle was used, set at 10°.

2.8. Surface roughness measurements

To visualize the surface deformation resulting from LP, profilometry was performed on the UPed and LPed specimens. Both specimens were ground using P220–P2400 grit SiC grinding papers, then polished with 3–1 μm diamond suspension and 0.05 μm colloidal silica. The LPed specimen was peened after the polishing process. Profilometry was performed using a KLA Tencor D-500 profilometer. The system was set to a 10 μm range using a scan speed of 0.10 mm/s. Data was collected at 2000 points/s and 16 data points were averaged and recorded to minimize noise from over sampling.

2.9. Raman spectroscopy analysis

Before oxidation, Raman spectroscopy was used to investigate potential contamination resulting from the LP process. Following high-temperature oxidation, Raman spectroscopy was used to identify phase constituents present in the oxide layer. The Raman spectra were obtained using a Horiba Jobin Yvon Inc. LabRAM HR800 at a wavelength of 532 nm with a 100 mW green laser. The grating was set to 950 grooves/mm and the laser power was set to 10 %. 6 accumulations of data at a 10 s acquisition time were averaged to generate the spectra for all specimens. Prior to all Raman spectroscopy analysis of the specimens, the system was calibrated following the standard calibration procedure for the equipment using a silicon wafer.

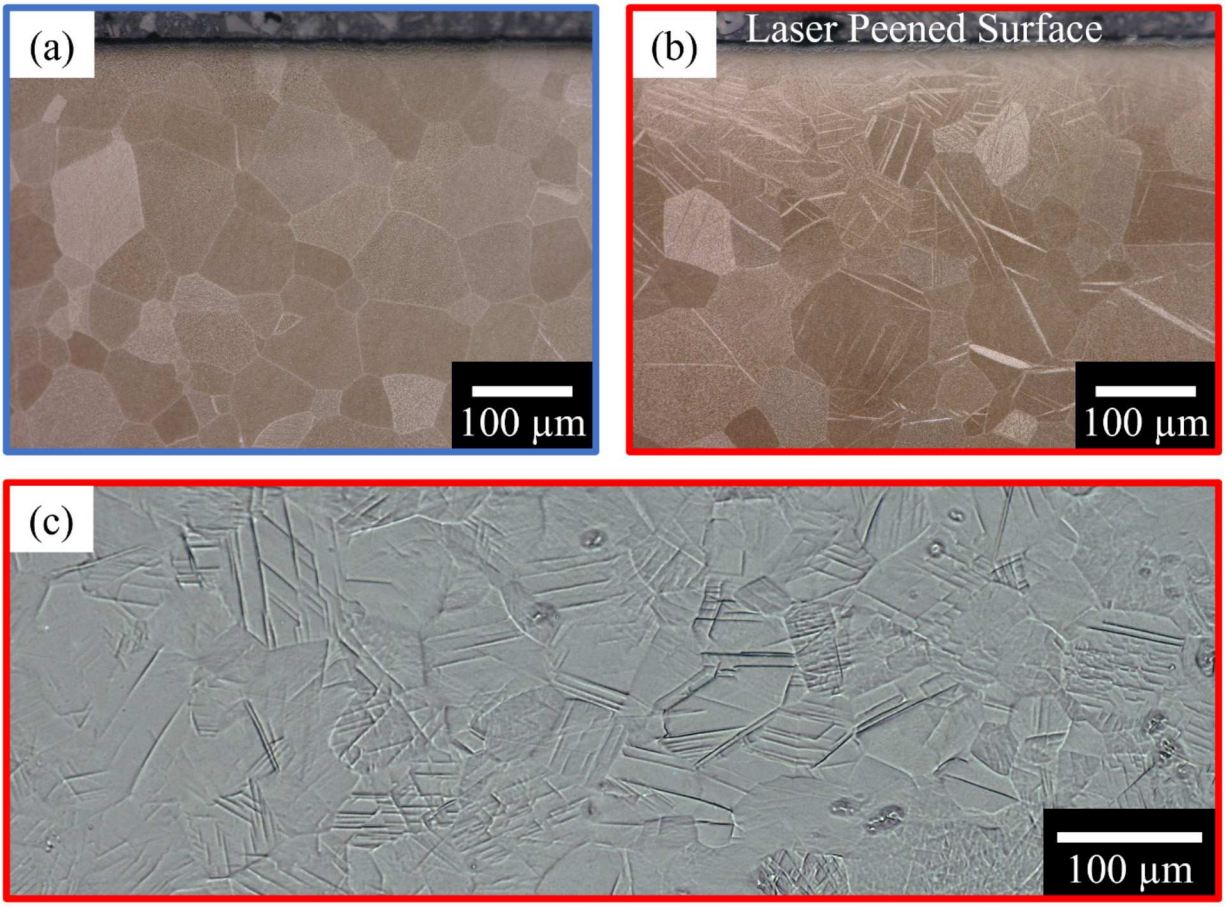

Fig. 2. OM images of cross-sectioned (a) UPed and (b) LPed Ti specimens after etching and prior to oxidation and (c) an HDR image of the treated surface following LP. No polishing or etching was performed on the LPed surface following LP.

3. Results and discussion

3.1. Analysis of specimens prior to high-temperature oxidation

3.1.1. Optical microscopy analysis (prior to oxidation)

The use of OM is a useful tool for visualizing the formation of twin defects that result from deformation occurring during the LP process. It is important to note that the specimens in Fig. 2(a) and (b) were ground and polished using the same process parameters to ensure direct comparisons could be made. The image included in Fig. 2(c) was obtained from the LPed surface following LP. This specimen was polished before LP to highlight changes to the affected surface as a result of the treatment. No additional surface preparation or etching was performed following LP. Compared to UPed specimen (Fig. 2(a)), the LPed specimens presented a high density of twins as shown in Fig. 2(b) and (c). Optical observation shows frequent occurrence of twin defects on the affected surface and the local sub-surface in Fig. 2(c) and (b), respectively. In this case, there are no signs of laser ablation (Fig. 2(c)) which can occur following LP when an ablative layer is not used. The highest density of twins can be observed near the affected surface in reduced frequency throughout the entire 400 μm depth in the cross section shown. For comparison, no twins are observed in the UPed specimen present in Fig. 2(a).

These deformation-induced twins act as a mechanism to reduce crack formation and propagation, which is a commonly desired result of the LP treatment. Many other studies have seen the similar formation of these twin defects as a result of deformation from the LP process [21,27,37,38]. As commercially-pure Ti (CP-Ti) has a hexagonal close packed (HCP) structure, deformation occurs by slip and twinning, however, HCP lattice structures limit slip modes available [38,39] and promote the formation of twin defects.

3.1.2. Microhardness measurements (prior to oxidation)

Microhardness data obtained from the Grade 1 Ti specimens before oxidation are included in Fig. 3(a–c). As twin defects contribute to increased strength and hardness [40], the most significant microhardness increase is found just below the LPed surface, where the density of deformation-induced twins is the highest. At a depth of 70 μm, microhardness is increased by 27.8 % when compared to the average UPed microhardness values (Fig. 3(a)). As seen in Fig. 2(b), the highest density of deformation-induced twins appears to be within the region 100–150 μm from the surface. In this same region, the largest increase in microhardness was measured (compare Fig. 2(b) to Fig. 3(a) and (c)). The high strain-rate resulting from LP promotes grain refinement and the generation of CRSs near the surface [31,40] which results in significant hardness increases in the affected regions [32,36,38]. One mechanism attributed to the increase in hardness is that plastic deformation (and accompanied dislocation motion) is inhibited by twin boundaries [40]. Additionally, increased CRSs oppose deformation and also contribute to increased hardness [41]. Since the pressure wave generated from LP dissipates as it moves through the material [32], the increase in microhardness in this study becomes less significant at a depth of ~130 μm; however, increased microhardness is observed throughout the entire ~460 μm cross-section. Up to ~460 μm from the surface, the average microhardness of the UPed specimen was 177.5 ± 7.4 HV, while the LPed specimen maintained an average microhardness of 195.0 ± 15.6 HV. Averaged data plotted in Fig. 3(a) shows maximum values of 182 ± 7 HV and 227 ± 20 HV for UPed and LPed specimens, respectively. Previous studies on metals and alloys have observed the depth at which hardening from LP is detected, with hardness increases detected at depths up to ~1500–2000 μm from the peened surface [32,36,38,42,43].

The contour maps in Fig. 3(b) and (c) present the microhardness

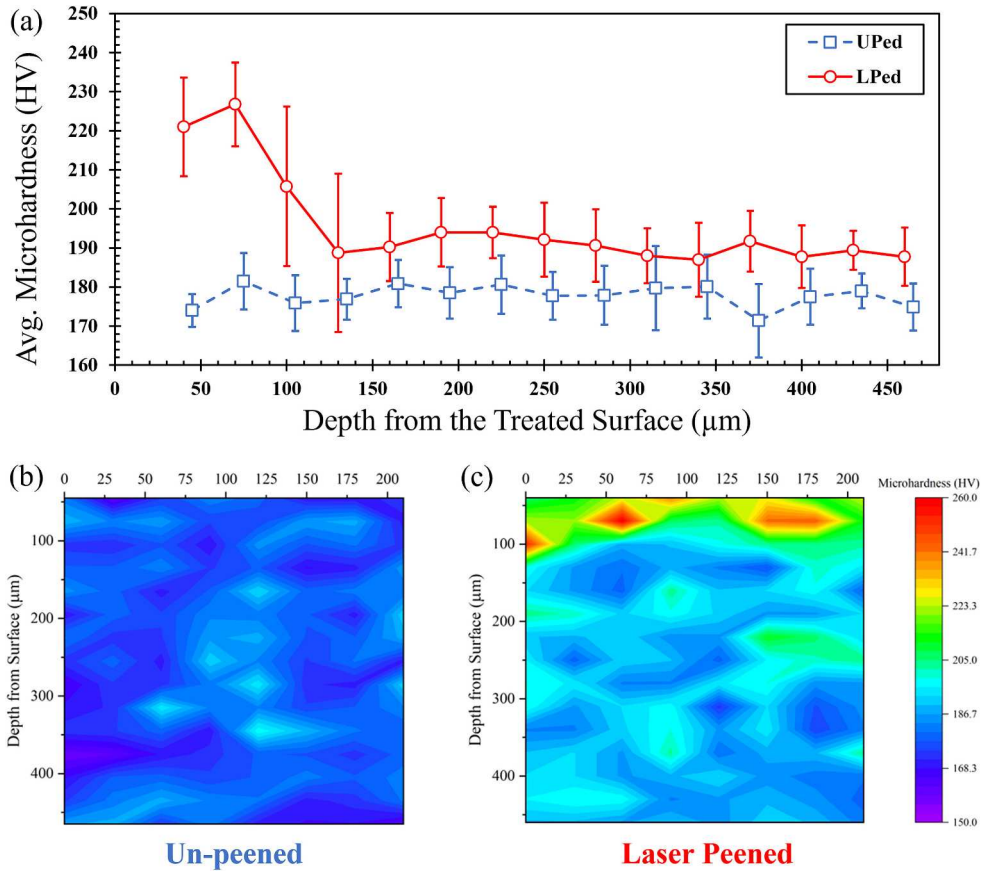

Fig. 3. (a) Microhardness profiles from the surfaces of the UPed and LPed specimens before oxidation and (b, c) microhardness contour plots used to produce the plot in (a).

distribution throughout the observed cross-sections. As expected, microhardness peaks close to the surface, but the contour plots reveal a consistent increase in microhardness throughout the cross-section. These visualizations help identify the deviation of microhardness data and highlight the uniformity of the hardness increase resulting from the LP process [36]. Comparison between the microhardness contour maps (Fig. 3(b) and (c)) and the OM images (Fig. 2(a) and (b)) show a correlation between hardness and observed twin density. Locations near the surface present frequent twins which are accompanied by increased microhardness values, supporting the hardening mechanism attributed to twin defects [38,39].

3.1.3. Residual stress analysis (prior to oxidation)

As mentioned previously, the deformation produced during the LP process generates CRSs on the surface and in the local sub-surface. To quantify the CRSs generated, XRD residual stress analysis (using the cos (α) method) has been performed on the LPed surface of the Ti specimen. The provided results indicate the formation of large CRSs on the LPed surface. The residual stress results from this experiment, and the results of similar studies investigating the residual stresses of LPed Ti-alloys are shown in Table 2 [32,39,44–46] – all of which are in-plane equibiaxial stresses oriented perpendicularly to the peening direction (parallel to the surface). It is noteworthy that both alloying elements and LP process parameters significantly influence residual stresses generated within the Ti-alloys from LP, however, consideration of other literature's findings affirms the validity of residual stress values obtained in this experiment.

In Fig. 3(a) and (c) maximum microhardness was achieved near the LP treated surface and dissipated with depth into the metal. As hardness increases are typically related to increases in compressive stresses, it is likely that the CRSs follow the same trend producing the maximum stress values near the surface before returning to a standard unstressed state. This is what has been discovered by other researchers which utilize XRD stress measurements with depth for LPed metals [43,47–49]. When the peak pressure produced by plasma during the LP treatment exceeds the Hugoniot elastic limit (HEL) of the LPed material, dynamic plastic deformation occurs, and CRSs are formed on the surface and sub-surface of the material [29,50]. The pressure generated by the treatment decreases as the pressure wave propagates through the material, and the generated CRS follows the same decreasing trend with depth [29,50].

It should be noted that residual stresses were not characterized following high-temperature exposure at 750 °C. At temperatures between 700 and 750 °C (annealing temperatures for this Grade 1 Ti) recrystallization occurs which causes residual stresses to relax as dislocations are rearranged and annihilated. In a similar study on the high-temperature oxidation resistance of Ti_2AlNb by He et al. [32], it was shown that compressive residual stresses imparted by LP in this Ti-alloy relaxed after just 4 h of heating at 720 °C. Similarly, Kanjer et al. [16] observed grain growth and recrystallization – phenomenon associated with residual stress relief – after only 10 h of exposure to 700 °C. This stress relaxation has also been reported in many other metals and alloys following high-temperature exposure when the temperature is ~$0.5T_m$ (where T_m is the melting temperature of the material – ~1600 °C in this case) [51].

3.1.4. Profilometry (prior to oxidation)

The LP treatment resulted in deformation of the affected surface, which is profiled in Fig. 4(a), where dimples created by the laser can be identified. It should be noted that the specimen used for profilometry was polished before LP treatment to reduce noise resulting from surface finish, highlighting the deformation caused by the treatment. An approximate spot size of 2 mm mapped by the profile validates the intended parameter for LP treatment. Fig. 4(a) shows the increase in surface roughness due to the LP treatment. Average roughness over the entire specimen increased from 0.027 ± 0.035 μm to 0.849 ± 0.985 μm, similar to results obtained by Joshi et al. [52], where average roughness was increased from 0.095 μm to 0.903 μm following LP at 8 GW/cm^2. This occurrence is expected as LP treatment induces deformation on the affected surface.

3.1.5. Raman spectrometry analysis (prior to oxidation)

Fig. 5 displays the Raman spectra obtained for the specimens prior to oxidation. The result is a low-intensity spectra that is nearly identical for both specimens. Few observable, but weak, peaks were observed in both recorded spectra, and the similarity of the UPed and LPed spectra suggests the LP treatment did not produce pronounced changes in the detected vibrational mode of molecules contained in the analyzed specimen. The two spikes in intensity (at ~140 cm^{-1} and ~212 cm^{-1}) could be attributed to the detection of a passive oxide formed at room temperature. The observed peak near 140 cm^{-1} could be attributed to the presence of both anatase and rutile phases [53,54] and the weak peak at approximately 212 cm^{-1} could correspond to the detection of brookite [55,56]. As the same two spikes appear in both spectra, the results suggest the absence of contamination from the LP process. Accordingly, results obtained during and after the oxidation process are likely a result of mechanical phenomenon, and without changes in chemical interaction.

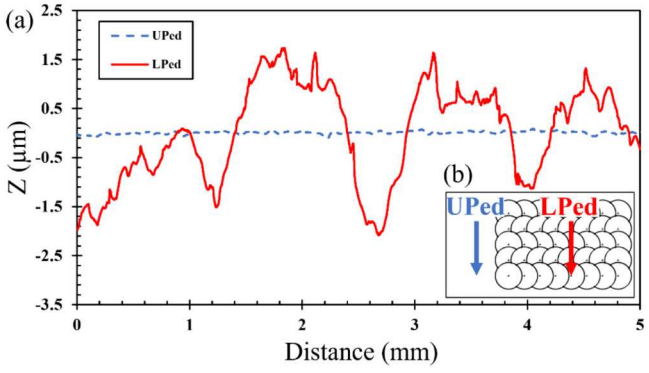

Fig. 4. (a) Line profiles from the UPed and LPed specimen's surfaces and (b) the profilometer path used to obtain these line profiles.

Table 2
Comparison of residual stress measurements following LP of similar titanium alloys.

	Current study	(CP-Ti) [39]	(Ti_2AlNb) [32]	(Ti-2.5Cu) [44]	(Ti-6Al-4V) [45]	(Ti-6Al-4V) [46]
LP power density (GW/cm^2)	10	6.5	13	5	10	9
LP overlap (%)	30	80 – longitudinal 30 – transverse	50	–	25	70
UPed (MPa)	52.8 ± 71.2	−77.1 ± 18.4	~0	–	134	50
LPed (MPa)	−301.9 ± 40.2 (surface)	−377.2 ± 42.5 (surface)	−387 (max, near surface)	−390 ± 16 (surface)	−296 (surface)	−400 (max, near surface)

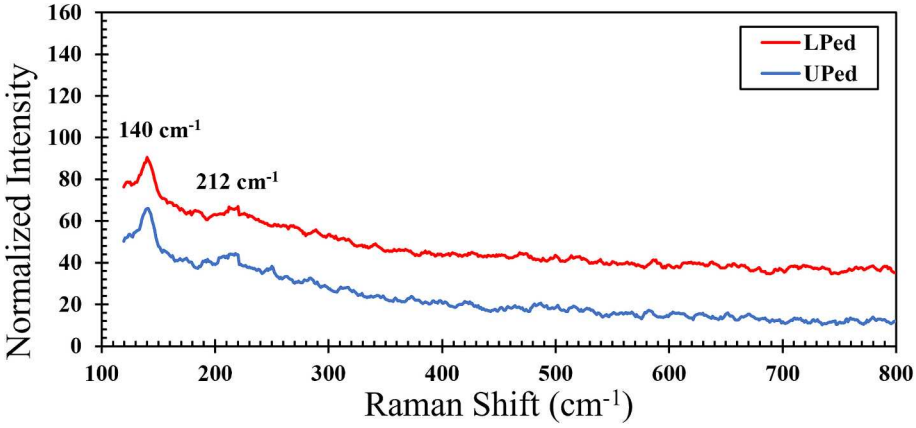

Fig. 5. Raman spectra obtained from the UPed and LPed specimen's surfaces. The spectra have been offset along the y-axis for ease of viewing, and an 8-point moving average has been applied to reduce noise.

3.2. Analysis of specimens following high-temperature oxidation

3.2.1. Thermogravimetric analysis (following oxidation)

The results from TGA indicate the viability of employing LP to reduce the mass gain of Grade 1 Ti in high-temperature oxygen containing atmospheres. To investigate the repeatability of the experiment, the mass gain of two un-treated specimens (UP-A and UP-B) and two LPed specimens (LP-A and LP-B) were recorded. Fig. 6(a–d) presents the oxidation kinetic curves obtained from 100 h oxidation of the Ti specimens at a temperature of 750 °C in an inert atmosphere consisting of 21 % oxygen and 79 % argon. At the end of the 100 h TGA analysis, UP-A and UP-B specimens experienced total normalized mass gains of 6.88 mg/cm^2 and 7.80 mg/cm^2, respectively. The LP-A and LP-B specimens experienced reduced total normalized mass gains of 6.33 mg/cm^2 and 5.08 mg/cm^2, respectively – on average, a reduction in mass gain of 22.28 % when compared to the un-treated (UP-A and UP-B) specimens. These results are similar to those reported by Kanjer et al. [21] in their pure oxygen TGA experiments, where their LPed specimens experienced a ~45 % reduction in mass gain following high-temperature oxidation at a temperature of 700 °C.

For oxidation of Ti, the general oxidation kinetics law (Eq. (1)) can be used to fit curves resulting from TGA [16,32,57].

$$\left(\frac{\Delta W}{A}\right)^{n} = k_n \bullet t \tag{1}$$

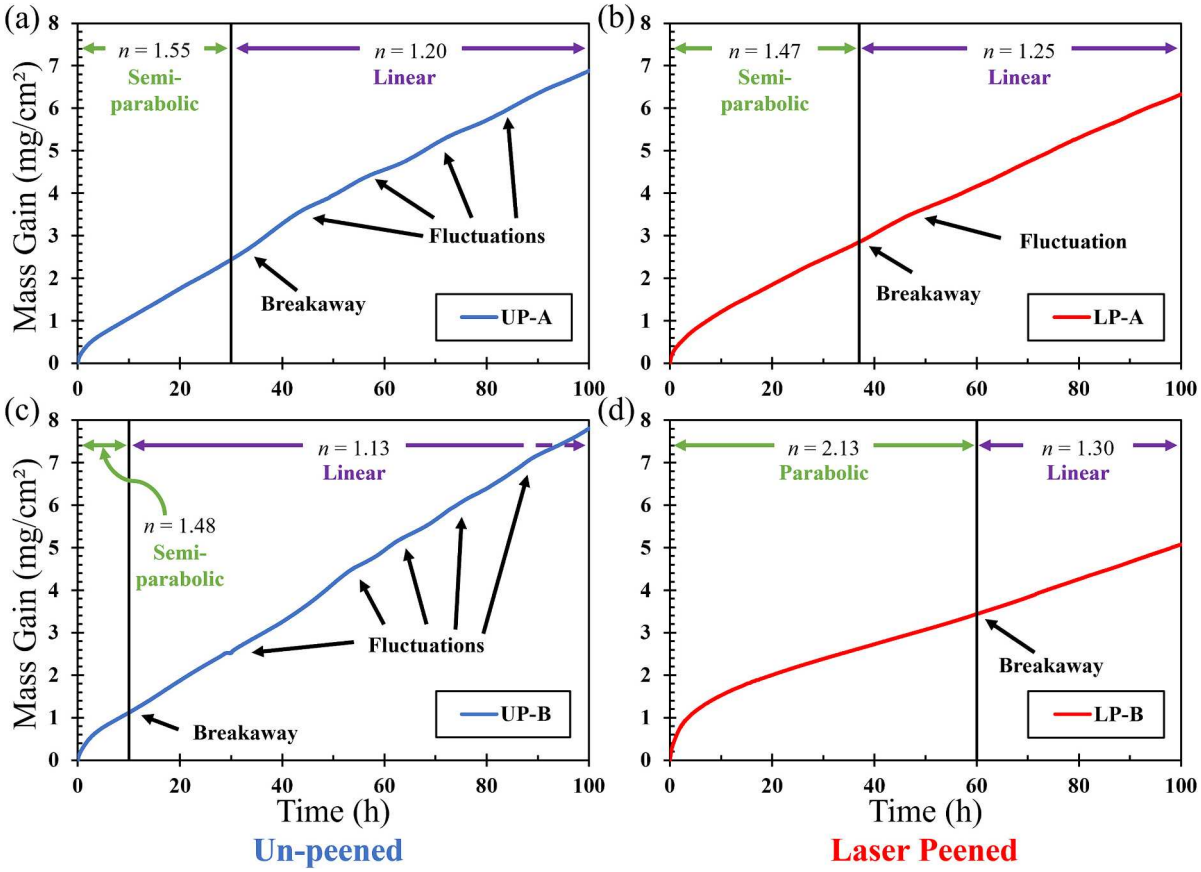

Fig. 6. Mass gain plots of the oxidation of (a) UP-A, (b) LP-A, (c) UP-B, (d) LP-B specimens during exposure to 750 °C in an argon and oxygen atmosphere.

where, ΔW is the weight gain, A is surface area of the specimen, k_n is the rate constant, t is time, and n is the oxidation law's degree index. The n parameter value is the combination of three processes that happen during oxidation time including: (1) oxide layer growth, (2) oxygen diffusion into the metal, and (3) the formation of imperfections in the oxide layer [21,58]. An n value of 2 correlates to parabolic law and suggests the presence of a protective oxide layer, which reduces the effective rate of oxygen diffusion [32,33].

In this study, initial stages of oxidation follow parabolic or semi-parabolic curves (see light-green annotations in Fig. 6(a–d)) before experiencing a breakaway shift towards linear mass gain (n ≈ 1 – see purple annotations in Fig. 6(a–d)). Fitting curves generated from the kinetics law to the initial stages yield n values of 1.55, 1.48, 1.47, and 2.13 for specimens UP-A, UP-B, LP-A, and LP-B, respectively. These values suggest some protective qualities of the oxide layer, with LP-B correlating best with parabolic law (Fig. 6(d)). Deviations in the linear and parabolic regions of the curves observed during TGA testing of the LPed specimens, as well as differences in mass gain (21.9 % difference), are likely attributed to inconsistencies in the specimen preparation (grinding and polishing) and the LP process. However, regardless of this, both LPed specimens exhibited larger regions of parabolic behavior – suggesting partial protection [32] – and subsequently lower total mass gain. Further observation of the curves reveals fluctuations in the rate of mass gain, which occur more frequently in the un-treated specimens.

The TGA results for the isothermal oxidation suggest the occurrence of three phenomena contributing to the mass gain curves as reported by Kanjer et el. [21]. They are as follows:

1. Rapid oxygen and Ti interaction (UP-A, UP-B, LP-A: ~0–2 h; LP-B: ~0–5 h)
   During this period, the initial processes of oxidation begin to occur. First, oxygen is adsorbed at the Ti surface. This oxygen is then absorbed into the Ti substrate through chemisorption or physical absorption. Once saturation occurs within the material, oxide nuclei are formed, and lateral growth of the oxide results in formation of an oxide scale. The oxide is classified as *n-type*, causing the growth of the oxide to occur inward respective of the metal/oxide interface [16,17]. In Fig. 6(d), it is clear that initially the LP-B specimen experienced more prolonged, rapid interaction with oxygen before the formation of a compact oxide scale.
2. Protective oxide barrier (UP-A: 2–30 h; UP-B: 2–10 h; LP-A: 2–37 h; LP-B: 5–60 h)
   As the oxide layer increases in thickness and density, it begins to mitigate oxidation of the titanium. The growth of this layer and the barrier it presents contribute to the parabolic shape of the mass gain curves. Significant enhancement of this protective layer is noticed in the LP-B specimen – characterized by an increased n value.
3. Oxide layer irregularities (UP-A: 30–100 h; UP-B: 10–100 h; LP-A: 37–100 h; LP-B: 60–100 h)
   Prolonged exposure to the high temperature eventually leads to the formation of irregularities within the oxide layer. Cracking on the outer surface of the oxide, and delamination of the layer reduces the effectiveness as a barrier to further oxidation. As new irregularities develop, oxidation occurs at a higher and more linear rate, without parabolic influence. These irregularities can also lead to inconsistent mass gain rates as specimens simultaneously experience the formation of imperfections and the formation of protective oxides where the substrate becomes exposed. This phenomenon can be observed in Fig. 6(a–d), where apparent changes in mass gain rate occur after breakaway (annotated as fluctuations).

The subsequent findings related to the cross-sections of the specimens (nanoindentation, microindentation, OM analysis, and SEM analysis) presented in this study exclusively pertain to the examination of UP-A and LP-A specimens, while results obtained from the surface of the oxide layer (Raman analysis and SEM of oxide layer) have been collected from UP-B and LP-B specimens.

3.2.2. Nanohardness measurements (following oxidation)

Nanoindentation hardness tests have been utilized to estimate the depth of oxygen diffusion and the formation of an α-case. Increased nanohardness detected in the pure Ti specimens indicates increased oxygen composition, as oxygen atoms occupy interstitial and substitutional sites [59]. The nanoindentation results shown in Fig. 7 show the LPed specimen produced lower nanohardness values near the surface suggesting a reduction in the amount of oxygen that has diffused into the Ti, contributing to the reduced mass gain seen in Fig. 6(a–d). In this experiment, similar nanohardness values were obtained deeper within the UPed specimen, and the nanohardness of the LPed specimen reverts to the average non-oxidized microhardness value of 177.5 ± 7.4 HV after reaching a depth of ~230 μm (compare Fig. 7 to Fig. 3(a)). In contrast, the UPed specimen maintains nanohardness above this level throughout the characterized depth. These findings imply that the LP treatment reduced the depth of oxygen penetration into the substrate.

Another important feature of the plot pertains to the error associated with indentations performed nearest to the surface. These large error bars are attributed to fracture of the α-case and inconsistent diffusion near the surface. In locations where a non-uniform or flawed oxide layer has formed, the rate of oxygen diffusion varies and can cause further embrittlement of the α-case, resulting in fracture and unpredictable hardness values. Both specimens show error bars due to this phenomenon, however, it appears to be more significant in the UPed specimen.

To support the claim of reduced oxygen diffusion observed in the LPed material, calculations can be performed to estimate diffusion coefficients. According to Fick's second law, diffusion can be modeled by the following differential equation [60]:

$$\frac{\partial C}{\partial t} = D\frac{\partial^2 C}{\partial x^2} \tag{2}$$

where D is diffusivity and C is the concentration of diffusing molecules. This relation relates the time rate of change of the composition to a profile of the concentration. If concentrations of the diffused medium are known, solving this relationship with the assumptions of constant surface concentrations and infinitely long medium allows for estimation of the diffusivity. Assuming oxygen concentration is directly proportional to hardness, Rosa [61] developed a relationship that can be used to solve for D:

$$\frac{H - H_0}{H_s - H_0} \propto 1 - erf\left(\frac{x}{2\sqrt{Dt}}\right) \tag{3}$$

where H refers to hardness values along the cross section, H_0 is the hardness at an infinite depth, and H_s is the surface hardness. For analysis in this paper, the average UPed specimen microhardness will be used as H_0, and nanohardness data closest to the surface will be ignored due to high uncertainty and the influence of fracture. H_s and D will be solved for simultaneously with the use of the solver feature in Excel, with the objective of minimizing the sum of the squares between calculated and experimental hardness values. The results yield H_s values of 1248 HV and 1176 HV for the UPed and LPed specimens, respectively. Also, a 34.6 % reduction in the diffusivity, D, from 1.15×10^{-10} cm^2/s (UPed specimen) to 7.52×10^{-11} cm^2/s (LPed specimen) was calculated for the LPed specimen. These results are plotted in Fig. 7.

3.2.3. Microhardness measurements (following oxidation)

The microhardness profiles obtained from the UPed and LPed specimens following high-temperature oxidation are includes in Fig. 8. Compared to results prior to oxidation (compare Figs. 3 and 8), the increase in microhardness resulting from the α-case formation is apparent, however, microhardness is nearly the same for oxidized (Fig. 8) and unoxidized (Fig. 3) specimens at depths greater than 230 μm. As expected,

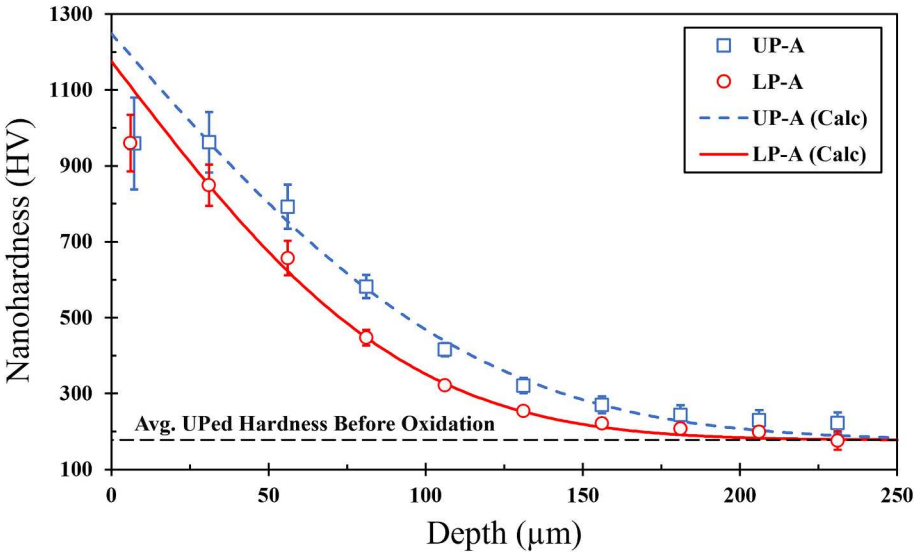

Fig. 7. Nanoindentation hardness profiles from the surfaces of the UP-A and LP-A specimens following high-temperature oxidation. Theoretical calculated hardness profiles are plotted as well.

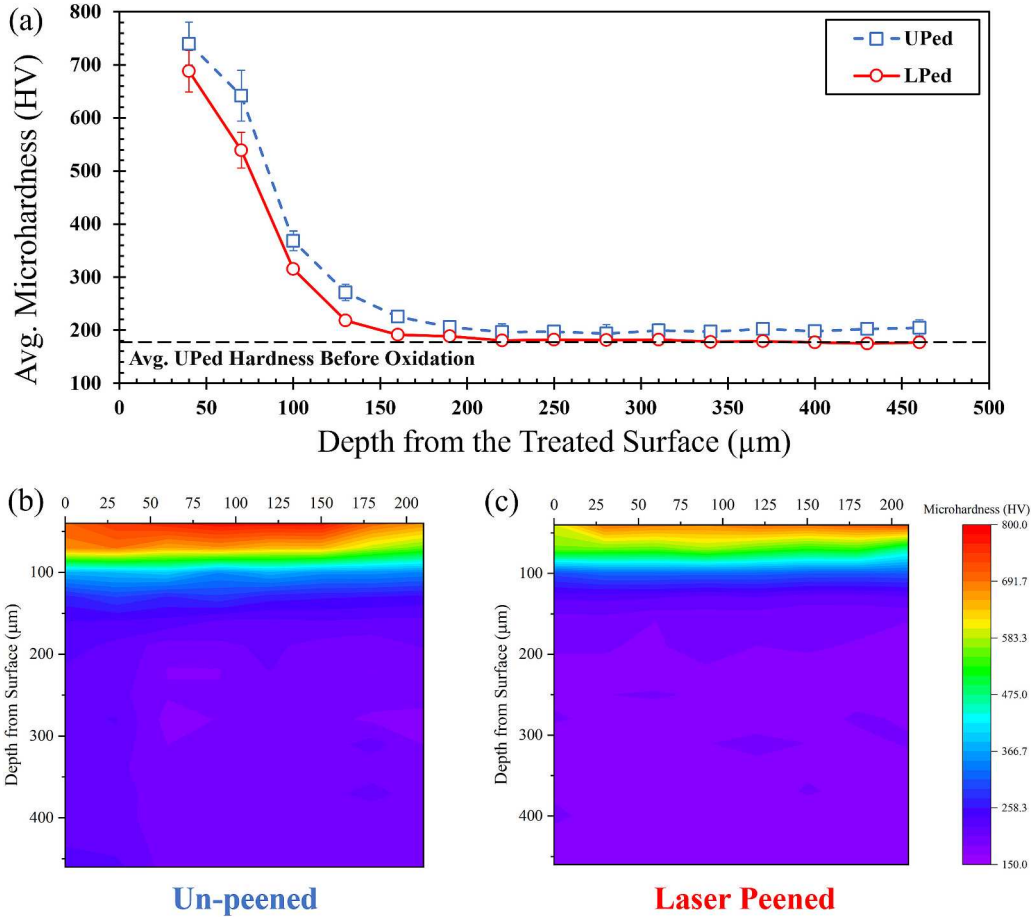

Fig. 8. (a) Microhardness profiles from the surfaces of the UPed and LPed specimens following oxidation and (b, c) microhardness contour plots used to produce the plot in (a).

the profile is similar to that measured during nanoindentation (Fig. 7), where a hardness gradient in observed throughout the α-case layer with respect to depth from the oxidized surface. Differences between the measured microhardness (Fig. 8) and nanohardness (Fig. 7) are the result of different measurement techniques. Nanoindentation creates smaller, more controlled, and more highly monitored indents when compared to microindentation [62]. This allows for precise characterization of hardness for a small area [62] and results in the measurement of higher nanohardness values near the surface (Fig. 7). Microindentation impressions are larger, capturing more of a material

gradient per indent resulting in less specific microhardness values (Fig. 8). Additionally, the reduction of α-case hardness, and thus oxygen diffusion in the LPed specimen is confirmed in Fig. 8. The contour maps in Fig. 8(b) and (c) provide an alternative visualization for the increased α-case microhardness noticed in the UPed specimen.

3.2.4. Optical microscopy analysis (following oxidation)

Fig. 9 presents images obtained during observation of the oxidized specimens' cross-sections using OM. Fig. 9(a) and (b) are images of the un-etched oxide interface regions while Fig. 9(c_1) and (d_1) are from the etched oxide interface regions. The main conclusion from these images is a reduction in overall oxide layer thickness, and a reduction in thickness of the visually apparent α-case layer (which can be observed as white in Fig. 9(c_1) and (d_1)). From optical observation of the entire specimens, the UPed specimen's oxide layer thicknesses ranged from 30 to 45 μm, whereas in the LPed specimen, oxide thicknesses were between 24 and 39 μm. Thin and densely formed oxide layers provide a protective layer between the atmosphere and the metal surface by inhibiting further oxidation [16] and the results from OM indicate improvement of this protective layer following LP. Furthermore, during the investigation of regions where oxide layer thicknesses were consistent between UPed and LPed specimens, a reduction in the observable α-case was noticed (compare Fig. 9(a) and (b)). The depth of this layer is visually estimated by a transition from a smooth to textured surface as seen in Fig. 9(c_1) and (d_1). At a location where both UPed and LPed specimens exhibited a 35 μm thick oxide layer, the α-case thickness appears to be reduced from ~91 μm to ~70 μm. This is in good agreement with the results of the nanoindentation and microindentation hardness tests (Figs. 7 and 8).

Fig. 9(c_1) and 9(d_1) presents lower magnification images of etched cross sections, highlighting a significant change in microstructure near the oxide interface region. Fig. 9(c_2) and (d_2) show the entire cross-sections of the UP-A and LP-A TGA specimens, respectively. When these images are compared to those of un-oxidized specimens (Fig. 2(a) and (b)), the increase in grain size is apparent. This observation confirms recrystallization and grain growth occurred during high-temperature oxidation at 750 °C for 100 h. This recrystallization and grain growth has also been observed by Kanjer et al. [16] after exposing Grade 1 Ti to 700 °C for only 10 h.

3.2.5. Scanning electron microscopy (following oxidation)

In order to examine fractures and irregularities in the oxidized specimens, SEM was employed to enhance spatial resolution and increase the depth of field, with the resulting micrographs displayed in Fig. 10(a–h). Fig. 10(a) and (b) showcases cross-sections of average well-formed oxide layers, revealing noticeable differences in thickness between the UPed and LPed specimens. In these micrographs, the LPed specimen exhibited a reduced oxide layer thickness, from 36 μm to 28 μm, with apparent improved adhesion of the oxide scale to the substrate. Additionally, irregularities (delamination and fracture of the TiO_2 as well as fracture of the α-case) can be identified in both cross sections (Fig. 10(c–f)). Fig. 10(c) and (d) depicts the delamination of the oxide layer, and Fig. 10(e) and (d) shows the addition of TiO_2 facture. Fractures and/or delamination of the oxide layer provide a less resistant path for oxygen to reach the Ti substrate, compromising its protective characteristics [16]. As such, these imperfections were frequently accompanied by fracture of the α-case. Severe α-case fracture was typically correlated with a non-uniform or disturbed oxide layer formed on the surface above the fracture, facilitating increased oxygen diffusion, and further embrittlement of the substrate. Despite the occurrence of these phenomena in both specimens, the frequency and severity of these features seemed to be reduced in the LPed specimen, however the observed difference may not be significant. Additionally, the oxide layer on the LPed specimen appears less porous and of a higher quality. In

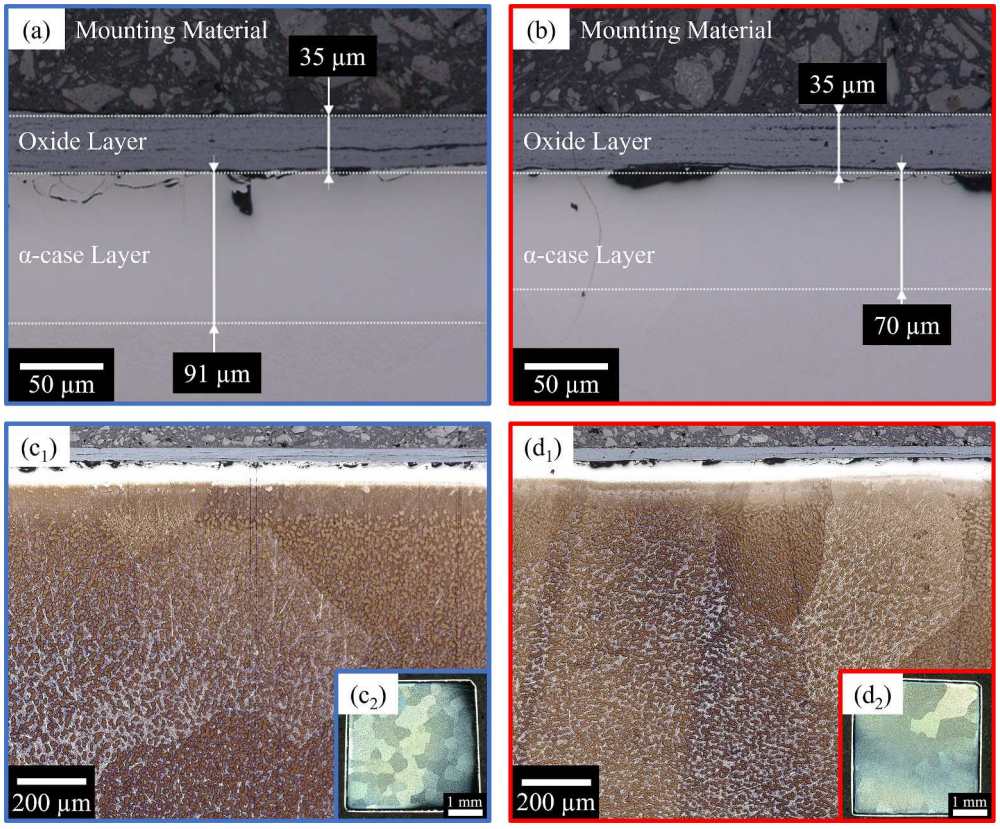

Fig. 9. OM images following high-temperature oxidation of cross-sectioned (a, c_1, c_2) UP-A and (b, d_1, d_2) LP-A specimens. (a, b) Cross-sectioned specimens before etching and (c_1–c_2, d_1–d_2) after etching. (c_2, d_2) Full cross-sectioned TGA specimens.

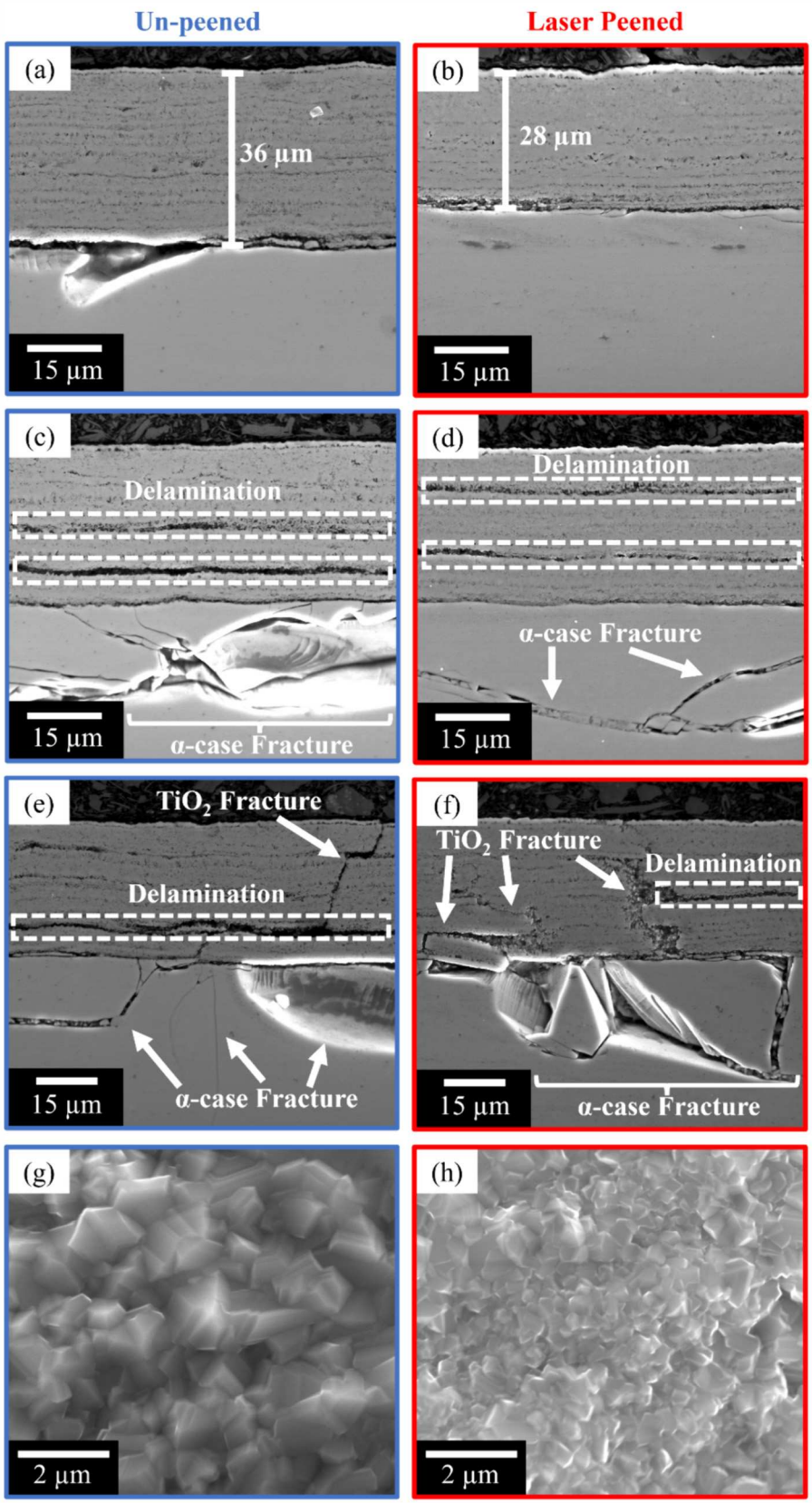

Fig. 10. SEM micrographs of the oxidized cross-sections of (a, c, e) UP-A and (b, d, f) LP-A specimens. Images in (g, h) are high-magnification micrographs from the outer surface of the oxide films on UP-B and LP-B specimens, respectively.

Fig. 10(a–d), the oxide layer on the LPed specimen is visually improved, especially towards the outermost layers (where the oxide layer first formed). To further investigate the quality of the oxide layer, SEM was also performed on the outer surface of the oxide layers. The corresponding micrographs are included in Fig. 10(g) and (h) and show substantial reduction in oxide particle size, likely contributing to increased density and compactness of the oxide layer on the LPed specimen. These characteristics influence the oxidation kinetics and enhance the protective performance of the oxide scale [32].

3.2.6. Raman spectroscopy analysis (following oxidation)

Spectra obtained from Raman spectroscopy analysis performed on the oxide layers of the specimens is presented in Fig. 11. The obtained spectra are well defined and present four distinct peaks, which were not observed before high-temperature oxidation. Compared to the results obtained before oxidation (shown in Fig. 5), the intensity of the recorded spectra in Fig. 11 are increased significantly (note the $\times 10^3$ intensity scale). In Raman spectra analysis, TiO_2 has active peaks within the 100–900 cm^{-1} range corresponding to active Raman modes of three phases of the oxide (rutile, anatase, and brookite) [53]. These resulting peaks obtained from the experiment indicate that the TiO_2 layer on the surface of both specimens is predominantly composed of the rutile phase. Significant peaks corresponding to rutile vibrational modes form at approximately 143, 447, and 610 cm^{-1} and are associated with B_{1g}, E_g, and A_{1g} vibrational modes, respectively [53]. Anatase has E_g, B_{1g}, and A_{1g} Raman detectible modes with peaks at 144, 197, 399, 516, and 639 cm^{-1} [54], however, the spectra does not show any identifiable peaks at these locations (other than near 144 cm^{-1}, however anatase is typically characterized by a more sharp and intense peak) indicating a low amount of the anatase phase. The peak at approximately 235 cm^{-1} could be attributed to disorder or second-order photon scattering – the result of multi-phonon phenomenon [53,63] – which is more intense in rutile than anatase phases [54]. The results of this study and comparison to other rutile Raman spectra are presented in Table 3 [53,63]. As seen in Table 3, the obtained results are in good agreement with previous research.

It has been reported by Ekoi et al. [53], that variations in peak positions correlate to differences in TiO_2 crystallite size. In their study, they identified an inverse linear relationship between E_g and A_{1g} peak positions and crystallite size. Based on these findings, the observed shifts in peak positions towards a higher wavenumber in both the E_g and A_{1g} modes in the LPed specimen's spectra implies a reduction in oxide particle size on the surface. These observations support the results obtained through SEM analysis of the oxide films (Fig. 10(g) and (h)) – with reduced oxide particle size observed on the outer oxide layer of the LPed specimen.

Table 3
Comparison of rutile peak positions obtained in this study with results from other literature.

UP-B	LP-B	Ekoi et al. [53]	Balachandran and Eror [63]	Assigned modes
142.0	142.0	143.2	144	B_{1g}
232.3	239.0	232.4	235	Multi-phonon
445.8	446.9	446.6	448	E_g
608.5	611.7	609.8	612	A_{1g}

The differences in peak intensities between the UP-B and LP-B specimens displayed in Fig. 11 indicate an increase in the detected rutile phase within the oxide layer on the LPed specimen. The relationship for the intensity of Raman scattered light is given in Eq. (4) [64]:

$$I(\nu)_R = \frac{2^4\pi^3}{45\cdot 3^2\cdot c^4}\cdot\frac{hI_L N(\nu_0-\nu)^4}{\mu\nu\left(1-e^{-\frac{h\nu}{kT}}\right)}\cdot\left[45\left(\alpha_a^{'}\right)^2+7\left(\gamma_a^{'}\right)^2\right] \quad (4)$$

where, c is the speed of light, h is Planck's constant, k is the Boltzmann constant, I_L is excitation intensity, T is absolute temperature, N is number of scattering molecules, ν_0 is laser excitation frequency, ν is molecular vibrational frequency, μ is reduced mass of the vibrating atoms, $\gamma_a^{'}$ is anisotropy invariant of the polarizability tensor, and $\alpha_a^{'}$ is mean value invariant of the polarizability tensor. $I(\nu)_R$ is the intensity integrated over the width of the Raman band; the area under the curve in Fig. 11. As the Raman parameters remained the same between the specimens analyzed in this study, the proportional relationship between integrated Raman intensity and N provides basis for quantitative analysis [64]. The higher values of intensity observed in the rutile Raman peaks (Fig. 11) correspond to a higher quantity of rutile molecules detected during the analysis. Assuming a proportional relationship, and using a trapezoidal integration approximation method, Raman detected 17.3 % more molecules in the LPed specimen than the UPed specimen. These results support the claim that the LPed specimen has formed a denser oxide layer on its surface.

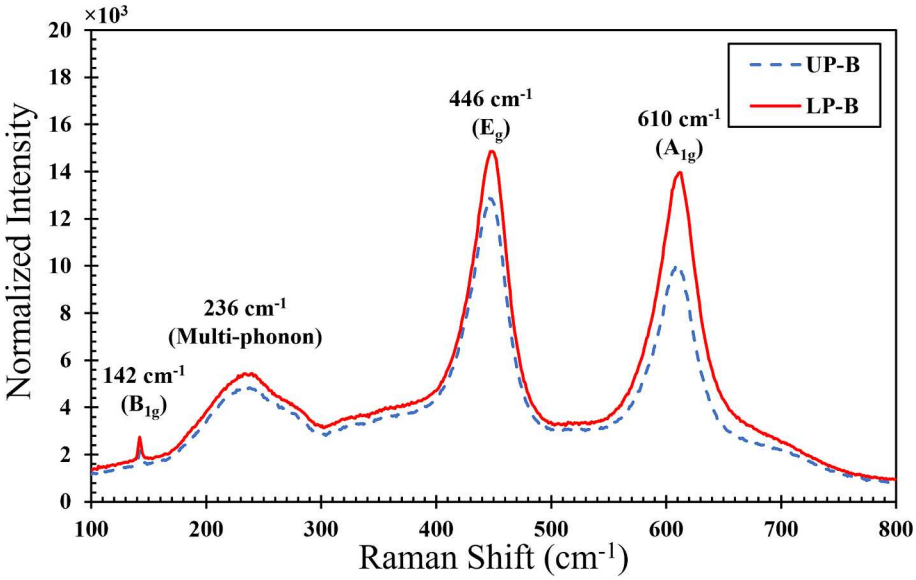

Fig. 11. Raman spectra obtained from the oxide layers of the UP-B and LP-B specimens.

3.3. Discussion

This study on the high-temperature oxidation resistance of Grade 1 Ti at 750 °C for 100 h in an oxygen atmosphere following LP has demonstrated the favorable characteristics LP can provide. The findings from the conducted experiments in this investigation can be outlined as follows:

1. Reduced mass gain during high-temperature oxidation resulting from LP.
2. Diffusion of oxygen into the Ti substrate is significantly reduced due to LP.
3. A more uniform and dense oxide scale resulting from LP better protects and reduces further oxidation of the Ti.

The mechanisms contributing to the beneficial changes in oxidation behavior result from the microstructural and mechanical alterations induced by the LP treatment. Before oxidation, it has been shown that LP produces twin defects up to significant depths, provides work hardening, and generates CRSs on the surface of the metal. Additionally, a reasonable surface was maintained, and there was no indication of chemical modification.

Previous studies [12,26] investigating the effect of LP on CP-Ti during high-temperature oxidation in dry air have attributed the favorable oxidation characteristics to the insertion of nitrogen in thin layers at the metal and oxide interface. This nitrogen is able to diffuse through the oxide layer more easily (due to its higher diffusion rate through rutile TiO_2) and creates a nitrogen enriched layer that slows down oxygen diffusion and reaction with the Ti substrate [12,26]. However, in this study, favorable changes in the oxidation process were able to be achieved without the presence of nitrogen. Kanjer et al. [26] had identified two other mechanisms that also likely contribute to the results obtained in this investigation. The first of which is related to the defects generated during the LP process. The high density of deformation-induced twins in the LPed specimen can promote increased oxygen diffusion during the initial stages of oxidation. In their paper, it was suggested that this occurrence allows for a quicker formation of oxide scale and supports the formation of the nitrogen enriched layer. This mechanism may also play a role without the presence of nitrogen, as increased oxygen diffusion during early stages of oxidation could facilitate the formation of a more protective oxide scale. Additionally, the initial establishment of a more oxygen-saturated layer may mitigate further diffusion of oxygen into the metal. The second mechanism is correlated to the effect of chemical reactivity in materials that have been mechanically treated. Gutman [65] has found that plastic deformation and subsequent stresses induced during the treatment of metals can lead to increased entropy, and as such, induce higher surface reaction rates. This would result in the speedier formation of the initial oxide layer, and more frequent reaction with oxygen. Both of these proposed mechanics fit well with the evidence displayed in this study. Fig. 6(a–d) clearly shows the increased initial mass gain for the LPed specimens, and the development of a more protective oxide layer than the one formed on UPed specimens. Increased interaction between Ti and oxygen would also have the effect of increasing the uniformity and density of the oxide layer, which is what was observed during SEM (Fig. 10(g) and (h)) and Raman spectrometry analyses (Fig. 11). Furthermore, a reduction in diffused oxygen and α-case depth would be expected and is supported by the results in Figs. 7–9.

4. Conclusion

In this study, the effects of a surface engineering treatment, namely LP, on the high-temperature oxidation behavior of pure (Grade 1) Ti have been investigated. High-temperature oxidation tests were carried out at 750 °C in a controlled inert atmosphere consisting solely of 79 % inert argon gas and 21 % oxygen. The impact of LP on the microstructural and mechanical properties of the Grade 1 Ti has been thoroughly investigated both before and after high-temperature oxidation. The results of this study are as follows:

- LP treatment produced plastic deformation near the surface of the Ti specimens, resulting in twin defects, increased hardness, the generation of CRSs, and increased surface roughness.
- Raman spectroscopy indicated that the LP process did not result in any chemical contamination.
- LPed specimens experienced reduced mass gain during high-temperature oxidation (22.3 % on average), with extended periods of protection before breakaway phenomenon and mass gain fluctuations were noticed.
- LP treatments reduced hardness in the α-case formed during high-temperature oxidation. This suggests a reduction in diffused oxygen. Additionally, utilizing a relationship between nanohardness and diffused oxygen, a 34.6 % reduction in the diffusion coefficient is estimated for LPed material.
- OM and SEM analyses showed a reduction in oxide and α-case layer thicknesses, with the discovery of decreased oxide particle size on the surface of the oxide formed on an LPed specimen.
- Raman spectroscopy produced higher intensity peaks when performed on the oxide layer of LPed material and integration suggests the detection of 17.3 % more molecules in the LPed oxide layer. This implies increased density of the layer, and increased protection during oxidation.

CRediT authorship contribution statement

Zachary Brown: Writing – original draft, Methodology, Data curation, Conceptualization. **Nicholas Brooks:** Writing – original draft, Formal analysis, Data curation. **Roxana Family:** Writing – original draft. **Mark Weaver:** Writing – review & editing, Resources. **Keivan Davami:** Writing – review & editing, Supervision, Resources, Funding acquisition.

Declaration of competing interest

The authors declare that they have no known competing financial interests or personal relationships that could have appeared to influence the work reported in this paper.

Data availability

Data will be made available on request.

Acknowledgements

This research was supported by the National Science Foundation (NSF), CMMI, Advanced Manufacturing Program (Award Number: 2029059). The authors would like to thank Alireza Doroudi at The University of Alabama for assistance with electron microscopy analysis. The authors also acknowledge the use of The University of Alabama's Core Analytical Facility (CAF). The authors gratefully acknowledge DURIP funding from the Air Force Office of Scientific Research (AFOSR).

References

[1] Jesús Jáquez-Muñoz, et al., Electrochemical corrosion of titanium and titanium alloys anodized in H_2SO_4 and H_3PO_4 solutions, Coatings 12 (3) (1 Mar. 2022) 325, https://doi.org/10.3390/coatings12030325.
[2] Thato Sharon Tshephe, et al., Additive manufacturing of titanium-based alloys - a review of methods, properties, challenges, and prospects, Heliyon 8 (3) (Mar. 2022), https://doi.org/10.1016/j.heliyon.2022.e09041.
[3] Wen Zhang, Xu. Jun, Advanced lightweight materials for automobiles: a review, Mater. Des. 221 (Sept. 2022) 110994, https://doi.org/10.1016/j.matdes.2022.110994.

[4] Francis Froes, et al. (Eds.), Titanium for Consumer Applications, 2019, https://doi.org/10.1016/c2017-0-03513-9.

[5] Liu, Ya'nan, et al., Optimization of microstructure and properties of composite coatings by laser cladding on titanium alloy, Ceram. Int. 47 (2) (Jan. 2021) 2230–2243, https://doi.org/10.1016/j.ceramint.2020.09.063.

[6] Chaolin Tan, et al., Progress and perspectives in laser additive manufacturing of key aeroengine materials, Int. J. Mach. Tool Manuf. 170 (Nov. 2021) 103804, https://doi.org/10.1016/j.ijmachtools.2021.103804.

[7] P. Zhao, et al., Wear and high-temperature oxidation resistances of AlNbTaZrX high-entropy alloys coatings fabricated on ti6al4v by laser cladding, J. Alloys Compd. 862 (May 2021) 158405, https://doi.org/10.1016/j.jallcom.2020.158405.

[8] Lujun Huang, et al., Multiscale architecture and superior high-temperature performance of discontinuously reinforced titanium matrix composites, Adv. Mater. 33 (6) (23 July 2020), https://doi.org/10.1002/adma.202000688.

[9] J. Alhammadi, et al., Enhancement of oxidation resistance in titanium by plasma treatment for high temperature applications, J. Phys. Conf. Ser. 2368 (1) (1 Nov. 2022) 012026, https://doi.org/10.1088/1742-6596/2368/1/012026.

[10] Jingjie Dai, et al., High temperature oxidation behavior and research status of modifications on improving high temperature oxidation resistance of titanium alloys and titanium aluminides: a review, J. Alloys Compd. 685 (Nov. 2016) 784–798, https://doi.org/10.1016/j.jallcom.2016.06.212.

[11] Siva Teja Sala, et al., Effect of laser peen forming process parameters on bending and surface quality of ti-6al-4v sheets, J. Mater. Process. Technol. 305 (July 2022) 117578, https://doi.org/10.1016/j.jmatprotec.2022.117578.

[12] L. Lavisse, A. Kanjer, P. Berger, P. Peyre, et al., Effect of mechanical surface treatments on the high temperature oxidation of pure titanium: the role of nitrogen, MATEC Web of Conferences 321 (2020) 12045, https://doi.org/10.1051/matecconf/202032112045.

[13] A.M. Chaze, C. Coddet, The role of nitrogen in the oxidation behaviour of titanium and some binary alloys, J. Less Common Metals 124 (1–2) (Oct. 1986) 73–84, https://doi.org/10.1016/0022-5088(86)90478-9.

[14] Christoph Leyens, Manfred Peters (Eds.), Titanium and Titanium Alloys: *Fundamentals and Applications*, WILEY, 2005.

[15] Vinod Deshmukh, et al., Removal of alpha case on titanium alloy surfaces using chemical milling, Mach. Sci. Technol. 21 (2) (3 Apr. 2017) 257–278, https://doi.org/10.1080/10910344.2017.1284558.

[16] Birhan Sefer, Oxidation and Alpha–Case Phenomena in Titanium Alloys Used in Aerospace Industry: Ti–6Al–2Sn–4Zr–2Mo and Ti–6Al–4V, Luleå University of Technology, 2014. Thesis.

[17] Gerd Lütjering, James C. Williams, Titanium, Eng. Mater. Proc. (2007), https://doi.org/10.1007/978-3-540-73036-1.

[18] George Zheng Chen, et al., Cathodic deoxygenation of the alpha case on titanium and alloys in molten calcium chloride, Metall. Mater. Trans. B 32 (6) (Dec. 2001) 1041–1052, https://doi.org/10.1007/s11663-001-0093-8.

[19] R. Gaddam, et al., Influence of alpha-case layer on the low cycle fatigue properties of ti-6al-2sn-4zr-2mo alloy, Mater. Sci. Eng. A 599 (Apr. 2014) 51–56, https://doi.org/10.1016/j.msea.2014.01.059.

[20] I. Gurrappa, et al., Influence of nitrogen implantation on the high temperature oxidation of titanium-base alloys, Surf. Coat. Technol. 201 (6) (Dec. 2006) 3536–3546, https://doi.org/10.1016/j.surfcoat.2006.08.106.

[21] Armand Kanjer, Virgil Optasanu, Luc Lavisse, María Del Marco de Lucas, Steeve Dejardin, et al., Influence of mechanical surface treatment on high-temperature oxidation of pure titanium, Oxid. Met. 88 (3–4) (3 Jan. 2017) 383–395, https://doi.org/10.1007/s11085-016-9700-6.

[22] Billy L. Crowder (Ed.), Ion Implantation in Semiconductors and Other Materials, 1973, https://doi.org/10.1007/978-1-4684-2064-7.

[23] G.H. Gleaves, et al., The effects of ion-implanted impurities on the anodic oxidation of titanium, J. Phys. F 7 (10) (Oct. 1977) 2031–2039, https://doi.org/10.1088/0305-4608/7/10/007.

[24] A. Ebach-Stahl, et al., Cyclic oxidation behaviour of the titanium alloys Ti-6242 and Ti-17 with Ti–Al–Cr–Y coatings at 600 and 700°C in air, Surf. Coat. Technol. 223 (May 2013) 24–31, https://doi.org/10.1016/j.surfcoat.2013.02.021.

[25] D.K. Das, S.P. Trivedi, Microstructure of diffusion aluminide coatings on ti-base alloy IMI-834 and their cyclic oxidation behaviour at 650 °C, Mater. Sci. Eng. A 367 (1–2) (Feb. 2004) 225–233, https://doi.org/10.1016/j.msea.2003.10.196.

[26] A. Kanjer, L. Lavisse, et al., Effect of laser shock peening on the high temperature oxidation resistance of titanium, Surf. Coat. Technol. 326 (Oct. 2017) 146–155, https://doi.org/10.1016/j.surfcoat.2017.07.042.

[27] V. Optasanu, et al., High temperature oxidation kinetics of shot-peened and laser-shock peened Ti-beta-21s, Oxid. Met. 96 (3–4) (20 July 2021) 257–270, https://doi.org/10.1007/s11085-021-10043-w.

[28] Kanjer, A., V. Optasanu, L. Lavisse, M. C. Marco de Lucas, P. Berger, et al. "Shot peening - performance." High Temperature Oxidation Behaviour of Titanium after Shot-Peening, https://www.shotpeener.com/library/pdf/2017040.pdf.

[29] Weiwei Deng, et al., Progressive developments, challenges and future trends in laser shock peening of metallic materials and alloys: a comprehensive review, Int. J. Mach. Tool Manuf. 191 (Oct. 2023) 104061, https://doi.org/10.1016/j.ijmachtools.2023.104061.

[30] Seiji Katayama (Ed.), Handbook of Laser Welding Technologies, Woodhead Publishing Limited, 2013.

[31] Abdullahi Gujba, Mamoun Medraj, Laser peening process and its impact on materials properties in comparison with shot peening and ultrasonic impact peening, Materials 7 (12) (10 Dec. 2014) 7925–7974, https://doi.org/10.3390/ma7127925.

[32] Dongsheng He, et al., Improvement in oxidation resistance of Ti_2AlNb alloys at high temperatures by laser shock peening, Corros. Sci. 184 (May 2021) 109364, https://doi.org/10.1016/j.corsci.2021.109364.

[33] L. Lavisse, A. Kanjer, P. Berger, V. Optasanu, et al., High temperature oxidation resistance and microstructure of laser-shock peened Ti-beta-21S, Surf. Coat. Technol. 403 (Dec. 2020) 126368, https://doi.org/10.1016/j.surfcoat.2020.126368.

[34] William F. Smith, Structure and Properties of Engineering Alloys, McGraw-Hill, 1981.

[35] Jon Dossett, George E. Totten (Eds.), ASM Handbook, Steel Heat Treating Fundamentals and Processes vol. 4A, ASM International, 2013.

[36] Nicholas Brooks, et al., Microstructural and mechanical characterization of pearlitic steel after high intensity laser peening and shot peening, Manuf. Lett. 38 (Nov. 2023) 35–39, https://doi.org/10.1016/j.mfglet.2023.09.004.

[37] P. Kofstad, High Temperature Corrosion, Elsevier Applied Science, 1988, pp. 289–299.

[38] J.Z. Lu, et al., Microstructural response and grain refinement mechanism of commercially pure titanium subjected to multiple laser shock peening impacts, Acta Mater. 127 (Apr. 2017) 252–266, https://doi.org/10.1016/j.actamat.2017.01.050.

[39] Angshuman Chattopadhyay, et al., Effect of laser shock peening on microstructural, mechanical and corrosion properties of laser beam welded commercially pure titanium, Opt. Laser Technol. 133 (Jan. 2021) 106527, https://doi.org/10.1016/j.optlastec.2020.106527.

[40] Jing Li, et al., Twin formation and its strengthening mechanism of pure titanium processed by cryogenic laser peening, Opt. Laser Technol. 120 (Dec. 2019) 105763, https://doi.org/10.1016/j.optlastec.2019.105763.

[41] Gonghou Yao, et al., A novel method for predicting residual stress in GH4169 machined surfaces through micro-hardness measurement, Appl. Sci. 13 (24) (14 Dec. 2023) 13257, https://doi.org/10.3390/app132413257.

[42] Michael Munther, et al., Laser shock peening and its effects on microstructure and properties of additively manufactured metal alloys: a review, Eng. Res. Exp. 2 (2) (1 June 2020) 022001, https://doi.org/10.1088/2631-8695/ab9b16.

[43] K. Praveenkumar, et al., Residual stress distribution and elevated temperature fatigue behaviour of laser peened Ti-6Al-4V with a curved surface, Int. J. Fatigue 156 (Mar. 2022) 106641, https://doi.org/10.1016/j.ijfatigue.2021.106641.

[44] E. Maawad, et al., Investigation of laser shock peening effects on residual stress state and fatigue performance of titanium alloys, Mater. Sci. Eng. A 536 (Feb. 2012) 82–91, https://doi.org/10.1016/j.msea.2011.12.072.

[45] Dileep Madapana, et al., Studies on laser shock peening on nanomechanical and mechano-chemical properties of titanium alloy (Ti6Al4V), JOM 75 (1) (10 Oct. 2022) 109–119, https://doi.org/10.1007/s11837-022-05504-9.

[46] A. Umapathi, S. Swaroop, Mechanical properties of a laser peened Ti-6Al-4V, Opt. Laser Technol. 119 (Nov. 2019) 105568, https://doi.org/10.1016/j.optlastec.2019.105568.

[47] Yi Lu, et al., The effects of laser peening on laser additive manufactured 316L steel, Int. J. Adv. Manuf. Technol. 107 (5–6) (Mar. 2020) 2239–2249, https://doi.org/10.1007/s00170-020-05167-3.

[48] Kangmei Li, et al., Formation mechanism of residual stress hole under different pulse durations and shock pressure distributions in Ti6Al4V alloy during laser peen texturing, Opt. Laser Technol. 130 (Oct. 2020) 106361, https://doi.org/10.1016/j.optlastec.2020.106361.

[49] F.Z. Dai, et al., Effect of laser spot size on the residual stress field of pure al treated by laser shock processing: simulations, Appl. Surf. Sci. 316 (Oct. 2014) 477–483, https://doi.org/10.1016/j.apsusc.2014.07.166.

[50] P. Peyre, R. Fabbro, Laser shock processing: a review of the physics and applications, Opt. Quant. Electron. 27 (12) (Dec. 1995) 1213–1229, https://doi.org/10.1007/bf00326477.

[51] O. Vöhringer, Relaxation of residual stresses by annealing or mechanical treatment, Adv. Surf. Treat. 4 (Jan. 1987) 367–396, https://doi.org/10.1016/B978-0-08-034062-3.50027-6.

[52] K. Sowmya Joshi, et al., Optimization of laser shock peening for titanium, Mater. Today: Proc. 5 (5) (2018) 12174–12186, https://doi.org/10.1016/j.matpr.2018.02.195.

[53] E.J. Ekoi, et al., Characterisation of titanium oxide layers using Raman spectroscopy and optical profilometry: influence of oxide properties, Results Phys. 12 (Mar. 2019) 1574–1585, https://doi.org/10.1016/j.rinp.2019.01.054.

[54] Toshiaki Ohsaka, et al., Raman spectrum of anatase, TiO_2, J. Raman Spectr. 7 (6) (Dec. 1978) 321–324, https://doi.org/10.1002/jrs.1250070606.

[55] G.A. Tompsett, et al., The Raman spectrum of Brookite, TiO_2 (Pbca, $Z = 8$), J. Raman Spectrosc. 26 (1) (Jan. 1995) 57–62, https://doi.org/10.1002/jrs.1250260110.

[56] Mariusz Dudek, et al., Changes in the laser-processed ti6al4v titanium alloy surface observed by using Raman spectroscopy, Materials 15 (20) (14 Oct. 2022) 7153, https://doi.org/10.3390/ma15207153.

[57] S. Frangini, et al., Various aspects of the air oxidation behaviour of a ti6al4v alloy at temperatures in the range 600–700 °C, J. Mater. Sci. 29 (3) (Feb. 1994) 714–720, https://doi.org/10.1007/bf00445984.

[58] P. Kofstad, et al., Investigation on the oxidation mechanism of titanium, Acta Chem. Scand. 12 (1958) 239–266, https://doi.org/10.3891/acta.chem.scand.12-0239.

[59] Nicholas Degnan, et al., Diffusion of oxygen in titanium, in: 2003 Annual Conference Proceedings, 2003, https://doi.org/10.18260/1-2–11928.

[60] David A. Porter, et al., Phase Transformations in Metals and Alloys, 8 Sept. 2021, https://doi.org/10.1201/9781003011804.

[61] Casimir J. Rosa, Oxygen diffusion in alpha and beta titanium in the temperature range of 932° to 1142°C, Metall. Trans. 1 (9) (Sept. 1970) 2517–2522, https://doi.org/10.1007/bf03038377.
[62] Esteban Broitman, Indentation hardness measurements at macro-, micro-, and nanoscale: a critical overview, Tribol. Lett. 65 (1) (Dec. 2016), https://doi.org/10.1007/s11249-016-0805-5.
[63] U. Balachandran, N.G. Eror, Raman spectra of titanium dioxide, J. Solid State Chem. 42 (3) (May 1982) 276–282, https://doi.org/10.1016/0022-4596(82)90006-8.
[64] M.J. Pelletier, Quantitative analysis using Raman spectrometry, Appl. Spectrosc. 57 (1) (Jan. 2003), https://doi.org/10.1366/000370203321165133.
[65] Emmanuel M. Gutman, Mechanochemistry of Solid Surfaces, Dec. 1994, https://doi.org/10.1142/2373.